ISSN 2682-681X (Paper), ISSN 2705-4241 (Online) | http://unilorinjoger.com | https://doi.org/10.63745/jogersi.2026.06.30.004

JOGER
SPECIAL ISSUE, 2026
JOURNAL OF GEOMATICS AND ENVIRONMENTAL RESEARCH
http://www.unilorinjoger.com

Geospatial Assessment of Mining Impacts on Environmental Resources Using Multi-Temporal SAR–Optical Data Fusion in Zamfara, Nigeria

Dahir M. Omar[1]*, Ayo Babalola[2], Oluwafemi O. Adeleke[3]

[1-2] Department of Surveying and Geoinformatics, University of Ilorin, Nigeria
[3] Department of Civil Engineering, University of Ilorin, Nigeria

*omar.dm@unilorin.edu.ng, dahirmomar@gmail.com | https://orcid.org/0000-0002-6202-3318

Abstract
Artisanal and small-scale gold mining (ASGM) has expanded markedly across Zamfara State since 2019, placing increasing pressure on vegetation, soils, and surface water systems. This study examined environmental change in four major mining LGAs, Anka, Bukkuyum, Maru, and Talata Mafara, using annual Sentinel-1 SAR and Sentinel-2 composites processed in Google Earth Engine (GEE) between 2019 and 2025. Fifty mine sites were validated through a multi-source framework combining Nigerian mineral maps, mining permit records, documentary evidence, and historical Google Earth Pro imagery. Environmental change was assessed within 250 m, 500 m, and 1 km buffers using Normalized Difference Vegetation Index (NDVI), Bare Soil Index (BSI), Modified Normalized Difference Water Index (MNDWI), Normalized Difference Built-up Index (NDBI), and Radar Vegetation Index (RVI), supported by Change Vector Analysis and Pearson correlation. Results reveal a landscape undergoing simultaneous mining expansion and ecological recovery. Mine-pit extent increased by 260% (2.54 – 9.16 ha), while reclaimed and revegetated surfaces expanded by 227% (945.89 – 3,096.15 ha). NDVI exhibited strong positive temporal correlations with cumulative mining expansion (r = 0.835 – 0.851), whereas MNDWI showed strong negative correlations (r = -0.814 to -0.839), indicating persistent vegetation transformation and declining surface-water conditions. RVI closely tracked vegetation disturbance and recovery patterns, with bare-surface extent peaking at 51.27 ha in 2024, corroborating both NDVI-derived degradation signals and subsequent revegetation trends. Cross-index analysis identified a strong inverse BSI – MNDWI relationship (r = -0.857 to -0.870), suggesting hydrological disruption extending beyond active excavation zones. NDBI demonstrated weak temporal relationships, reflecting the transient nature of mining settlements. The integrated SAR–optical framework provides a robust, scalable, and operational approach for monitoring ASGM impacts in data-scarce dryland environments.

ARTICLE INFORMATION
Received: 18 May 2026
Revised: 30 May 2026
Accepted: 31 May 2026
Published: 15 June 2026

KEYWORDS
artisanal Mining;
environmental degradation;
Google Earth Engine;
SAR-optical fusion;
Sentinel

Citation: Omar, D. M., Babalola A., Adeleke, O. O. (2026). Geospatial Assessment of Mining Impacts on Environmental Resources Using Multi-Temporal SAR–Optical Data Fusion in Zamfara, Nigeria. *Journal of Geomatics and Environmental Research*, Special Issue, 1(1), Pp 57-77.

1.0 INTRODUCTION

Artisanal and small-scale mining (ASM) is among the most spatially extensive drivers of land-cover change in sub-Saharan Africa, with well-documented cascading effects on ecosystem services, food security, and rural livelihoods (Hilson, 2002; Bansah *et al*., 2018). In Zamfara State, northwestern Nigeria, a gold mining expansion that accelerated sharply from 2019 onward has transformed large stretches of the semi-arid landscape. Rising global mineral commodity prices, especially for gold, coupled with the continuing erosion of traditional agricultural livelihoods, have drawn large numbers of operators into mining activities. As a result, Anka, Bukkuyum, Maru, and Talata Mafara Local Government Areas now constitute the most intensively mined corridor within the region. The result has been rapid proliferation of artisanal pits, open excavations, and rudimentary processing infrastructure, with land-cover consequences operating at a pace and scale that administrative reporting has been unable to track (Bartrem *et al*., 2022).

The environmental pathways of unregulated ASM are established across multiple biomes. Open-pit extraction strips vegetation cover, disrupts topsoil structure, and introduces heavy metals and chemical reagents into adjacent water bodies (Barde *et al*., 2024; Isah *et al*., 2025). In Zamfara, specifically, gold processing leaves behind wastewater and tailings with lead, cadmium, and other metal concentrations well above WHO limits, posing direct ecological and public health risks to communities in Anka and Maru (Barde *et al*., 2024; Oseikhuemen *et al*., 2025). Within the Sudano-Sahelian climatic zone that characterises Zamfara, these dynamics compound pre-existing vulnerabilities: the region's semi-arid soils are already susceptible to erosion and desertification, and the natural vegetation has limited capacity for self-recovery once removed (Balogun *et al*., 2024; Sambe *et al*., 2026). Despite the documented urgency of these processes, systematic spatial monitoring of mining impacts in Zamfara remains sparse. Existing studies are largely field-based, geographically constrained, and unable to capture degradation gradients across the full extent of affected LGAs over multiple years.

Satellite remote sensing offers a scalable and cost-effective route to large-area environmental monitoring in data-scarce regions. Sentinel-1 Synthetic Aperture Radar (SAR) and Sentinel-2 multispectral imagery provide co-registered 10-metre imagery at no cost, covering both cloud-penetrating microwave and spectrally rich optical channels. Their complementarity is operationally significant here: optical imagery in Zamfara is degraded during the harmattan season by persistent dust haze, while SAR alone cannot discriminate between mining-stripped soil and natural bare outcrops of similar surface roughness (Gao *et al*., 2018). Integrating both sensor types generates more robust evidence base than either alone, and a growing body of work demonstrates that SAR–optical fusion substantially improves land degradation detection in semi-arid environments where single-sensor approaches are inadequate (Ngom *et al*., 2022; Sengani *et al*., 2023).

Translating this multi-sensor, multi-year dataset into a spatially exhaustive analysis at 10-metre resolution across four LGAs would exceed the practical limits of desktop GIS environments, where local storage, processing memory, and download bandwidth become binding constraints as data volume grows. Google Earth Engine (GEE) resolves this bottleneck by co-locating analysis with the data archive in Google's cloud infrastructure, enabling server-side compositing, index computation, spatial reduction, and export operations across petabyte-scale imagery collections through a browser-based code editor and JavaScript API (Gorelick *et al*., 2017). GEE's integration of the Sentinel-1 and Sentinel-2 catalogues within a single harmonised environment, combined with built-in functions for cloud masking, median compositing, and vector-based spatial statistics, made it the natural execution platform for the multi-step analytical workflow described in this study. The platform's reproducibility, as a GEE script encodes every processing decision as shareable, version-controlled code, also supports the transparency and replicability objectives of the research.

Several spectral and radar indices have established track records in ASM impact assessment. NDVI captures vegetation health and detects mining-induced canopy loss (Tucker, 1979), though mining environments require threshold recalibration because excavated minerals and kaolinite clays create elevated soil brightness that compresses index values toward those of sparse vegetation (Ngom *et al*., 2020). BSI exploits shortwave-infrared sensitivity to mineral composition and soil moisture, enabling discrimination of active mining footprints from naturally bare surfaces (Castaldi *et al*., 2023). RVI, derived from Sentinel-1 cross-polarisation ratios (Mandal *et al*., 2020), provides a cloud-independent structural vegetation signal that operates independently of optical interference; its utility for vegetation monitoring in SAR time series is well established (Hu *et al*., 2024). MNDWI tracks surface water change and identifies spectral signatures consistent with sediment-laden tailing ponds (Xu, 2006), while NDBI captures built-up expansion associated with mining population influx (Zha *et al*., 2003).

Prior West African studies have applied remote sensing to mine-impact assessment (Aryee *et al*., 2003; Couttenier *et al*., 2022; Dao *et al*., 2024), and recent reviews confirm that reliable spatial information on ASM locations remains largely unavailable owing to the informal and unlicensed nature of most operations (Ngom *et al*., 2022). Few studies, however, have combined SAR-optical data fusion with multi-index, multi-temporal analysis at the local scale. Critically, no study to date has systematically characterised the full 2019–2025 environmental trajectory of the Zamfara corridor during its most intensive expansion phase. This study addresses these gaps through four research questions:

i. How have vegetation cover, soil condition, surface water, and settlement extent changed within and around mining sites across the four LGAs between 2019 and 2025?
ii. What spatial gradient of degradation is detectable at 250 m, 500 m, and 1 km from known mine sites?
iii. How strongly does SAR-derived surface disturbance correlate with multi-index environmental degradation signals across buffer zones?
iv. How consistently do RVI (SAR-based) and NDVI (optical-based) characterise mining-induced vegetation loss under dust-affected conditions?

This study also demonstrates that Google Earth Engine can support a reproducible SAR-optical fusion workflow for local-scale environmental monitoring in a data-scarce West African setting.

2.0 STUDY AREA

The study area encompasses four Local Government Areas in Zamfara State, northwestern Nigeria: Anka, Bukkuyum, Maru, and Talata Mafara (Figure 1). These LGAs lie within a Precambrian mineral-bearing geological belt of the Zamfara Sahel that hosts the most active artisanal gold mining corridor in the country (Ado *et al*., 2022), and all four have documented histories of pit excavation, open-cut workings, and rudimentary processing activity that intensified markedly from 2019 onward (Bartrem *et al*., 2022; Oseikhuemen *et al*., 2025). Fifty mine sites were identified and validated across the four LGAs, with Anka carrying the highest concentration (24), followed by Bukkuyum (12), Maru (9), and Talata Mafara (5); field geochemical sampling in Anka and Maru has confirmed heavy metal contamination consistent with active processing activity (Barde *et al*., 2024).

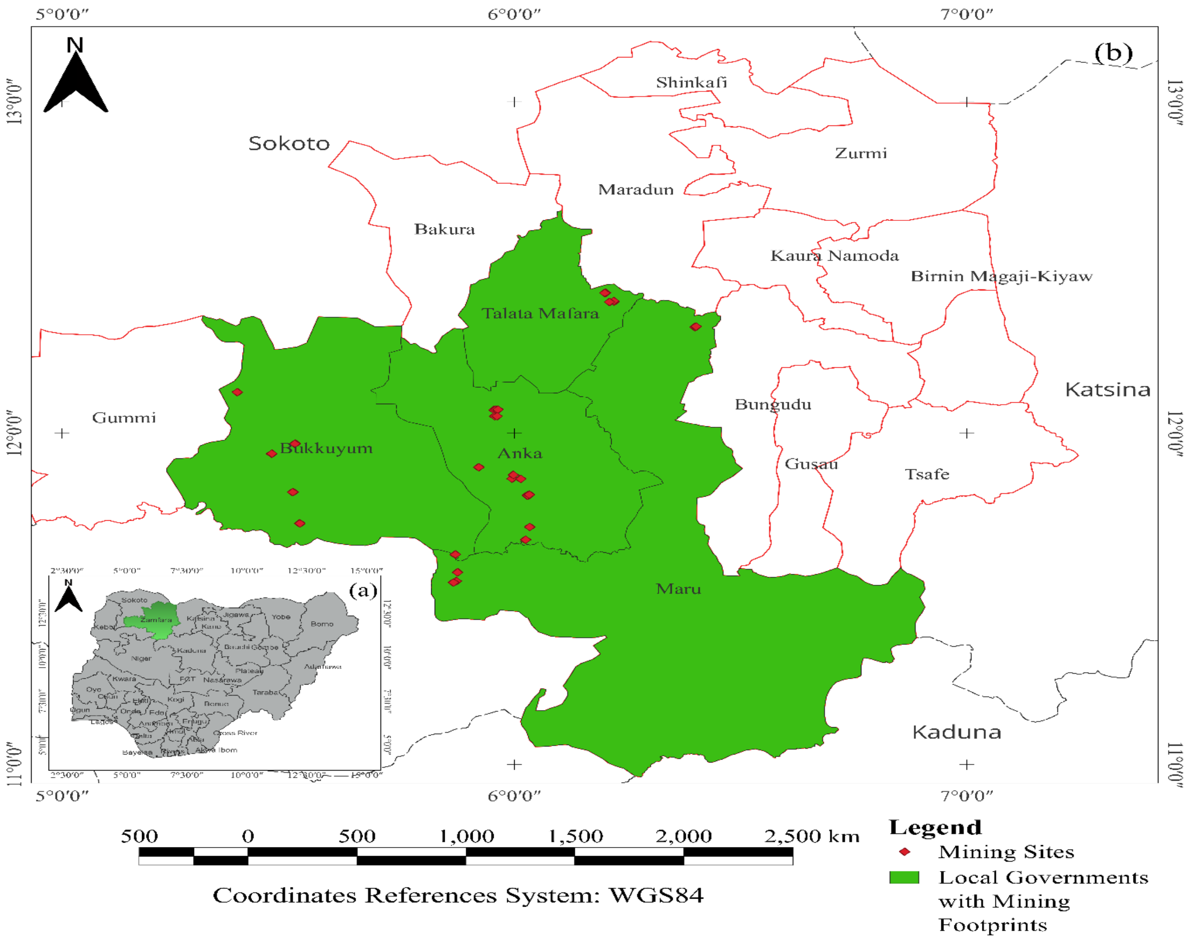

Figure 1: Study area map showing (a) Zamfara State within Nigeria, (b) the four study LGAs (Anka, Bukkuyum, Maru, and Talata Mafara), and the 50 validated mine site locations.

The region falls within the Sudano-Sahelian climatic zone, characterised by a single rainfall season (June - September, mean annual precipitation 700 - 900 mm) and a prolonged dry season (October-May) during which northeasterly harmattan winds carry mineral dust that substantially reduces optical remote sensing data quality (Sambe *et al*., 2026). Zamfara is among the frontline states most severely affected by desertification in Nigeria, with pre-existing semi-arid soils that are highly susceptible to erosion and have limited recovery capacity once stripped of vegetation cover (Sambe *et al*., 2026). Natural vegetation is predominantly Sudan savanna, comprising wooded, shrubby, and grassy savanna strata with sparse tree cover, transitioning to degraded scrubland in heavily mined areas (Ado *et al*., 2022). Terrain is gently undulating, ranging from approximately 300 m to 600 m above sea level, and is dissected by seasonal river channels that support localised riparian vegetation and serve as water sources for artisanal processing operations.

3.0 DATA AND METHODS

3.1 Data Sources

The study draws on two categories of data: satellite remote sensing imagery for environmental index computation and change detection, and ancillary reference datasets for mine site identification, topographic context, and population characterisation (Table 1). All satellite data were accessed through the Google Earth Engine catalogue and processed server-side without local download.

The primary remote sensing inputs are the Sentinel-1 Ground Range Detected (GRD) and Sentinel-2 Surface Reflectance Harmonized products, both provided by the European Space Agency (ESA) through the Copernicus Open Access Programme at 10-metre spatial resolution. Sentinel-1 GRD offers dual-polarisation (VV and VH) C-band SAR backscatter acquired in Interferometric Wide Swath mode, providing cloud- and haze-independent surface characterisation across the full 2019 - 2025 study period (Torres *et al*., 2012). Sentinel-2 SR Harmonised supplies 13-band multispectral surface reflectance at 10 - 20 metre resolution; the harmonised product reconciles radiometric differences between Sentinel-2A and Sentinel-2B sensors to ensure temporal consistency across annual composites (Phiri *et al*., 2021). Together, these two sensors form the SAR-optical data fusion core of the analytical framework. Topographic context is provided by two digital elevation models: the 30-metre SRTM DEM from USGS, used for terrain characterisation, and the 30-metre Copernicus GLO-30 DEM, used as a cross-check for slope and drainage delineation. The Global Human Settlement Layer (GHSL) Population Grid from the Joint Research Centre (JRC) at 100-metre resolution and 2020 epoch provides settlement-density context for interpreting NDBI-derived built-up changes around mine sites.

The reference datasets underpin the mine site identification and validation workflow. The Mineral Resources Map of Nigeria, published by the Nigerian Geological Survey Agency (NGSA) at a 1:2,500,000 scale, provided the geological basis for constraining the study area to LGAs overlying gold-bearing formations. Mining permit records obtained from the Nigeria Mining Cadastre Office (NMCO) supplied a spatially registered list of licensed and recently lapsed concessions within the four LGAs, narrowing the candidate site inventory to permit polygons and their surrounding areas. These administrative sources were supplemented by published academic literature and news reporting, which captured unlicensed workings absent from the formal permit record. Final site coordinates were validated in Google Earth Pro using the historical imagery time-slider to confirm surface disturbance signatures at each candidate location. The full dataset inventory is summarised in Table 1.

Table 1. Dataset Inventory

S/N	Dataset	Source	Spatial Resolution	Temporal Coverage
1	Sentinel-1 GRD	ESA Copernicus	10 m	2019 - 2025
2	Sentinel-2 SR Harmonized	ESA Copernicus	10 m	2019 - 2025
3	SRTM DEM	USGS	30 m	Static
4	GLO-30 DEM	Copernicus	30 m	Static

S/N	Dataset	Source	Spatial Resolution	Temporal Coverage
5	GHSL Population Grid	JRC	100 m	2020 epoch
6	Mineral Resources Map of Nigeria	Nigerian Geological Survey Agency (NGSA)	1:2,000,000	2023 Edition
7	Mining Permit Records	Nigeria Mining Cadastre Office (NMCO)	Tabular/Vector	24/05/2026
8	Mine Site Points (validated)	Google Earth Pro + Field Verification	Vector	2024
9	Mining POI (supplementary)	Published Literature and News Sources	Vector	2024

3.2 Mine Site Identification and Validation

Fifty mine site locations were identified and validated through a sequential four-stage protocol designed to triangulate evidence from geological, administrative, documentary, and remote sensing sources.

Stage 1 - Geological screening. The Mineral Resources Map of Nigeria, published by the Nigerian Geological Survey Agency (NGSA) was used to delineate LGAs overlying gold-bearing geological formations in Zamfara State. This spatial filter established the geologically plausible extent of artisanal gold mining and constrained subsequent investigation to four LGAs: Anka, Bukkuyum, Maru, and Talata Mafara.

Stage 2 - Permit-based narrowing. Mining permit records held by the Nigeria Mining Cadastre Office (NMCO) were examined to identify licensed or previously licensed exploration and small-scale mining concessions within the four LGAs. Active and recently lapsed permits provided a spatially registered initial candidate list of sites where legal or semi-legal mining operations had been formally recorded, narrowing the search area from the full LGA extents to specific permit polygons and surrounding zones.

Stage 3 - Documentary corroboration. Published academic literature and news media reporting on artisanal mining activity in the selected LGAs were reviewed to cross-check and supplement the permit-derived candidate list. This step was particularly important for capturing unlicensed artisanal workings that fall outside the NMCO permit framework but have been documented in investigative or scientific reporting.

Stage 4 - Google Earth Pro visual validation. Each candidate site was individually examined in Google Earth Pro using the historical imagery time-slider tool to review the site's appearance across multiple acquisition dates spanning the study period. Sites were confirmed as active or recently active mine locations only where characteristic surface signatures of artisanal excavation visible pit scarring, stripped bare-soil haloes, spoil heaps, or tailings deposits- were identifiable in high-resolution satellite imagery at or before 2025. This step served as the primary spatial ground-truthing mechanism, anchoring each confirmed site to a verified coordinate. Representative examples of the visual signatures used to confirm mine sites across the four LGAs are shown in Figure 2.

3.3 Processing Framework

All processing was conducted on the Google Earth Engine (GEE) cloud computing platform (Gorelick *et al*., 2017). GEE provides direct server-side access to the full Sentinel-1 and Sentinel-2 archives, eliminating the need to download, store, or pre-process raw imagery locally, a prerequisite for this study given the imagery required to build seven annual composites across four LGAs at 10-metre resolution. Processing operations, including cloud masking, median compositing, index computation, buffer zone reduction, and change vector differencing, were implemented as GEE JavaScript scripts, each operation executed in parallel across Google's distributed computing infrastructure. This approach compressed multi-step workflows that would take days on a workstation to minutes and ensured that all analytical decisions are encoded in reproducible, shareable script form. Annual dry-season composites (January - April) were generated for each year from 2019 to 2025. The dry-season window was chosen deliberately: it avoids rainy-season cloud cover while holding vegetation phenological state approximately constant across years, ensuring that inter-annual index differences reflect land-condition change rather than seasonal flux.

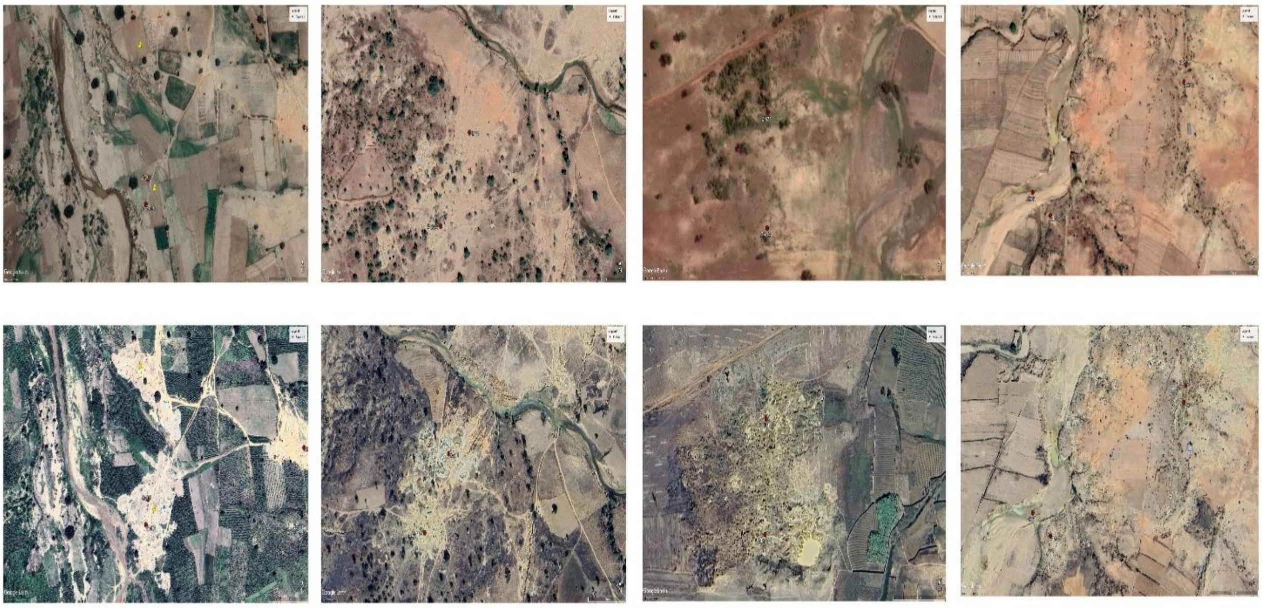

Figure 2. Google Earth Pro high-resolution satellite imagery showing some of the validated mine sites (Before Mining and After Mining) (Source: Google Earth).

a. **Sentinel-1 SAR Ground Range Detected (GRD) imagery** in Interferometric Wide Swath mode was filtered to ascending orbit passes with dual VV - VH polarisation. Median compositing reduced speckle noise. Backscatter values (dB) were converted to a linear power scale before RVI computation to avoid mathematical artefacts in ratio-based indices.
b. **Sentinel-2 Optical Level-2A Surface Reflectance Harmonized imagery** was filtered to scenes with cloud fraction below 20%. Median compositing produced cloud-free annual mosaics. Band digital numbers were scaled to surface reflectance by dividing by 10,000 before index computation.

3.4 Spectral and Radar Indices

The following indices were computed annually across the 2019 - 2025 time series:

Normalised Difference Vegetation Index (NDVI) (Tucker, 1979)**:**

$$NDVI = \frac{B8-B4}{B8+B4} \qquad \text{Equation 1}$$

A five-class scheme calibrated for mining environments was applied to annual NDVI images (Ngom *et al*., 2020):

Class	NDVI Range	Interpretation
1	≤ 0.00	Mine pits and tailings ponds
2	0.00–0.12	Active excavation and infrastructure
3	0.12–0.22	Degraded buffer vegetation
4	0.22–0.45	Reclaimed or revegetating surfaces
5	> 0.45	Undisturbed baseline vegetation

Bare Soil Index (BSI) (Castaldi *et al*., 2023)**:**

ISSN 2682-681X (Paper), ISSN 2705-4241 (Online) | http://unilorinjoger.com | https://doi.org/10.63745/jogersi.2026.06.30.004

$$BSI = \frac{(B11+B4)-(B8+B2)}{(B11+B4)+(B8+B2)}$$ Equation 2

Modified Normalised Difference Water Index (MNDWI) (Xu, 2006)**:**

$$MNDWI = \frac{B3-B11}{B3+B11}$$ Equation 3

Normalised Difference Built-up Index (NDBI) (Zha *et al*., 2003)**:**

$$NDBI = \frac{B11-B8}{B11+B8}$$ Equation 4

Radar Vegetation Index (RVI) (Mandal *et al*., 2020)**:**

$$RVI = \frac{4 \cdot VH_{lin}}{VV_{lin}+VH_{lin}}$$ Equation 5

where $VV_{lin} = 10^{VV_{dB}/10} and VH_{lin} = 10^{VH_{dB}/10}$. RVI approaches 0 over bare or actively disturbed surfaces and approaches 1 over dense, healthy vegetation (Hu *et al*., 2024).

3.5 Buffer Zone Analysis

Three concentric buffer zones were delineated around all documented mine site locations: Zone 1 (0 - 250 m, direct impact), Zone 2 (250 - 500 m, near impact), and Zone 3 (500m - 1 km, far impact) (Figure 3). Mean index values were extracted annually per zone using spatial reduction at a 30 m analysis scale, enabling quantification of the environmental degradation gradient as a function of proximity to mining activity.

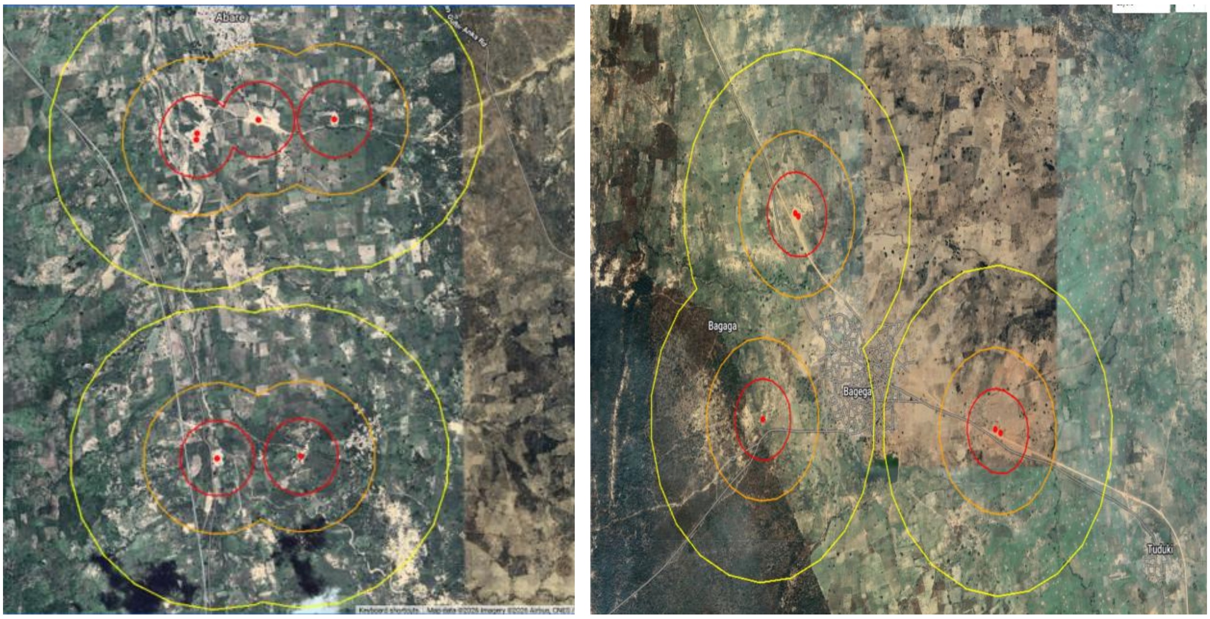

Figure 3. Sample of the buffer zone (Zone 1 (Direct Impact) – Red, Zone 2 (Near Impact) – Brown, Zone 3 (Far Impact) – Brown) (Source: Google Earth)

3.6 Change Vector Analysis

A per-pixel difference image was computed for each index between the 2019 baseline and the 2025 terminal year, following the Change Vector Analysis framework (Lambin & Strahler, 1994):

$$\Delta Index = Index_{2025} - Index_{2019}$$

Pixels with ΔNDVI < -0.3 were classified as rapid excavation zones, indicating severe vegetation loss consistent with open-pit mining. An independent RVI difference image flagged SAR-confirmed vegetation-loss zones where ΔRVI < -0.1. Spatial co-occurrence of both flags provided a multi-sensor convergence mask for highest-confidence degradation mapping (Salih *et al*., 2017).

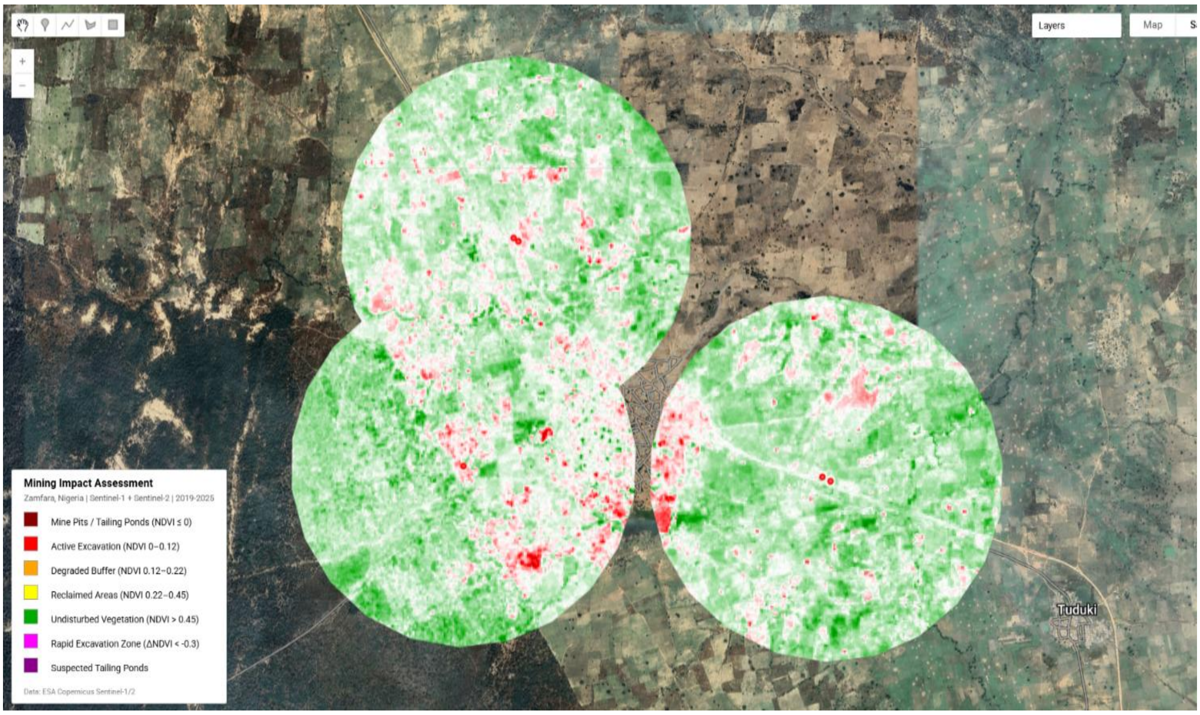

Figure 4. Change Vector Analysis ΔNDVI between 2019 and 2025

3.7 Correlation Analysis

SAR VV backscatter change ($\Delta VV = VV_{2025} - VV_{2019}$) served as a proxy for surface disturbance intensity, with increased backscatter reflecting the rougher, disrupted surfaces associated with excavation. Buffer zones established around the 50 validated mine site locations provided the spatial stratification framework for sampling. A stratified random sample of 1,000 points was drawn across the study area, distributed across the three buffer zones. Pearson correlation coefficients (r) were computed between ΔVV and each of $\Delta NDVI, \Delta BSI, \Delta MNDWI, \Delta NDBI, and\ \Delta RVI$. Distance-to-mine was also computed for each sample point to quantify the spatial decay of index change with proximity to mining activity. Scatter plots with linear trendlines and R^2 values were generated for all index combinations.

4.0 RESULTS AND DISCUSSION

4.1 Vegetation Loss (NDVI and RVI)

The annual Normalised Difference Water Index (NDVI) time series reveals a more complex trajectory than a simple monotonic decline. Mean Zone 1(Direct) NDVI rose from 0.1608 in 2019 to 0.2027 in 2025, an increase of +0.042, while Zone 2 (Near) increased from 0.1697 to 0.2187 (+0.049) and Zone 3 (Far) from 0.1726 to 0.2269 (+0.054) (Table 2 and Figure 5). The trend across all zones is directionally similar, a moderate dip in 2022 followed by progressive gains in 2023 - 2025, and the gradient from Zone 1 to Zone 3 is preserved throughout, with Zone 1 consistently returning the lowest NDVI values. These patterns reflect the compound influence of mining-related land disturbance at the mine site level and broad-scale vegetation dynamics driven by inter-annual rainfall variability across the Sudano-Sahelian landscape. The net NDVI increase at the landscape scale does not preclude highly localised vegetation stripping at individual mine sites; rather, it underscores why mine-pit-specific class mapping is essential to isolate the mining signal from background climatic variation.

Table 2. Annual Mean NDVI

NDVI Time Series				
S/N	**Zone 1 (Direct)**	**Zone 2 (Near)**	**Zone 3 (Far)**	**Year**
1	0.160802664	0.169709421	0.172569744	2019
2	0.162966419	0.171608664	0.175839192	2020
3	0.173138019	0.182671236	0.185923316	2021
4	0.161063286	0.170038495	0.17347361	2022
5	0.174989821	0.182979188	0.186840134	2023
6	0.18151131	0.196322073	0.207751467	2024
7	0.202739452	0.218703449	0.226897079	2025

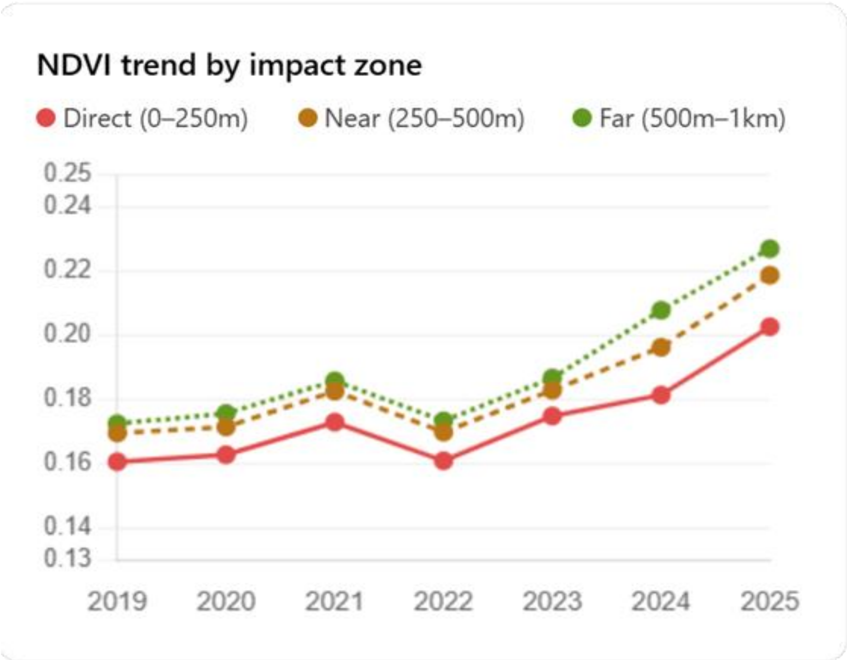

Figure 5. Annual Mean NDVI per buffer Zone, 2019 - 2025

NDVI class mapping captures the mine-site-specific dimension of change. Mine pit area (Class 1, NDVI ≤ 0.00) expanded from 2.54 hectares (ha) in 2019 to 9.16 ha by 2025, a 260.0% increase, with the most rapid pit formation occurring in 2022 - 2023 when pit area nearly doubled from 3.83 ha to 6.46 ha. Active excavation and infrastructure (Class 2, NDVI 0.00–0.12) declined from 520.04 ha to 233.94 ha over the same period, reflecting consolidation of pit surfaces rather than contraction of mining activity. More strikingly, reclaimed and revegetated surfaces (Class 4, NDVI 0.22 - 0.45) expanded from 945.89 ha in 2019 to 3,096.15 ha in 2025 (+227.3%), and undisturbed baseline vegetation (Class 5, NDVI > 0.45) rose from 4.48 ha to 106.18 ha (Table 3 and Figure 6). This trajectory indicates that while new pits continue to be excavated, substantial areas disturbed in earlier years are progressing through recovery or have been subject to post-mining revegetation. The coexistence of expanding pit area and expanding reclaimed area is consistent with the rotational pattern of artisanal mining, where pits are abandoned after alluvial gold is exhausted and secondary vegetation rapidly colonises exposed soils under favourable rainfall (Blanche *et al*., 2024; Ibukun *et al*., 2025).

ISSN 2682-681X (Paper), ISSN 2705-4241 (Online) | http://unilorinjoger.com | https://doi.org/10.63745/jogersi.2026.06.30.004

Table 3. NDVI class area statistics by year (2019–2025)

NDVI Class Area Time Series (ha)						
S/N	**Mine Pits**	**Active Excavation**	**Degraded Buffer**	**Reclaimed**	**Undisturbed**	**Year**
1	2.544237395	520.0425178	5788.29739	945.892763	4.483677408	2019
2	2.135584418	333.2713636	6045.016223	878.92416	1.913253974	2020
3	3.824097921	189.2489465	5786.334286	1272.30044	9.552814098	2021
4	3.825966998	419.4609014	5948.34766	882.266717	7.359340724	2022
5	6.456802575	229.7840148	5699.358549	1318.32159	7.339626105	2023
6	4.950933981	323.9590773	4717.610582	2119.68193	95.05806318	2024
7	9.158822255	233.9445367	3815.832972	3096.1457	106.1785584	2025

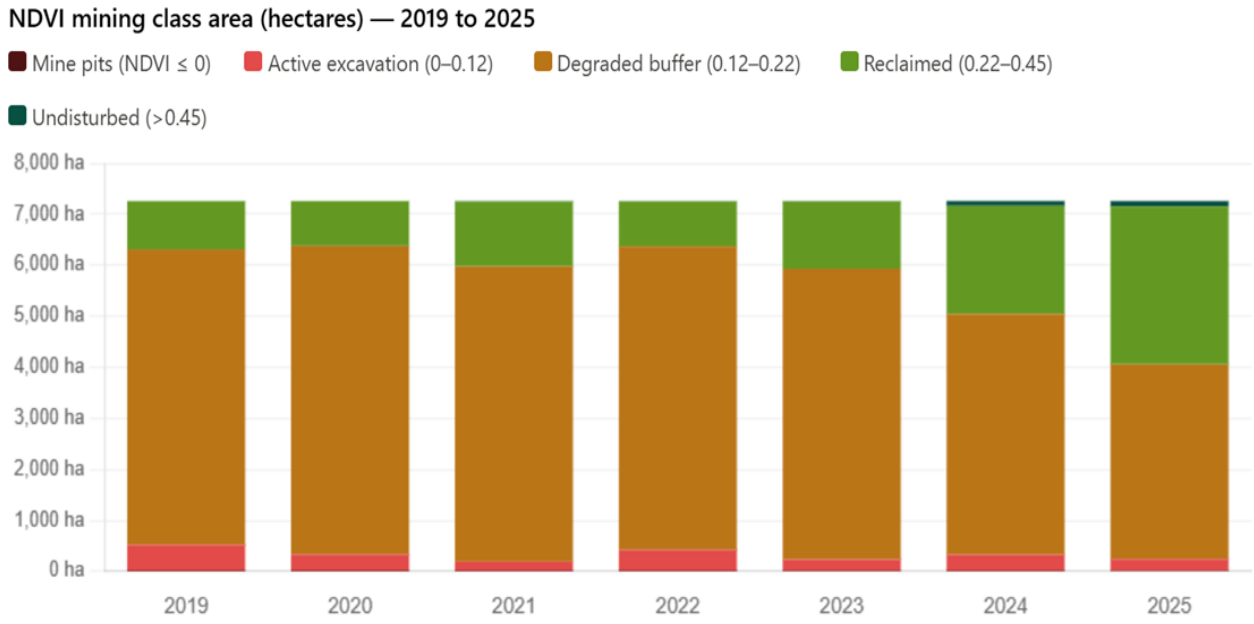

Figure 6a: NDVI class area statistics (ha) by year (2019–2025)

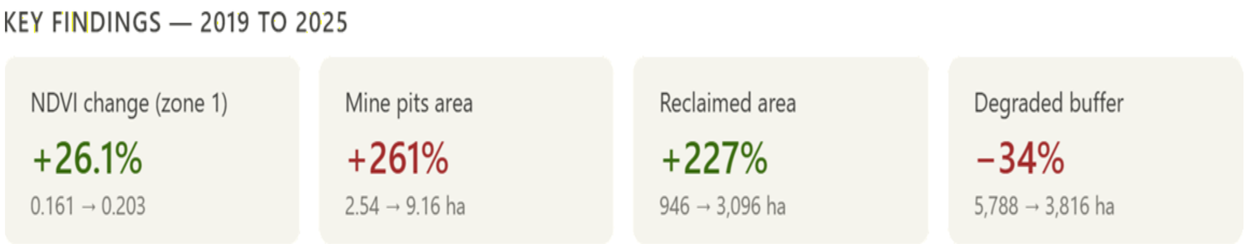

Figure 6b: NDVI Analysis Changes

ISSN 2682-681X (Paper), ISSN 2705-4241 (Online) | http://unilorinjoger.com | https://doi.org/10.63745/jogersi.2026.06.30.004

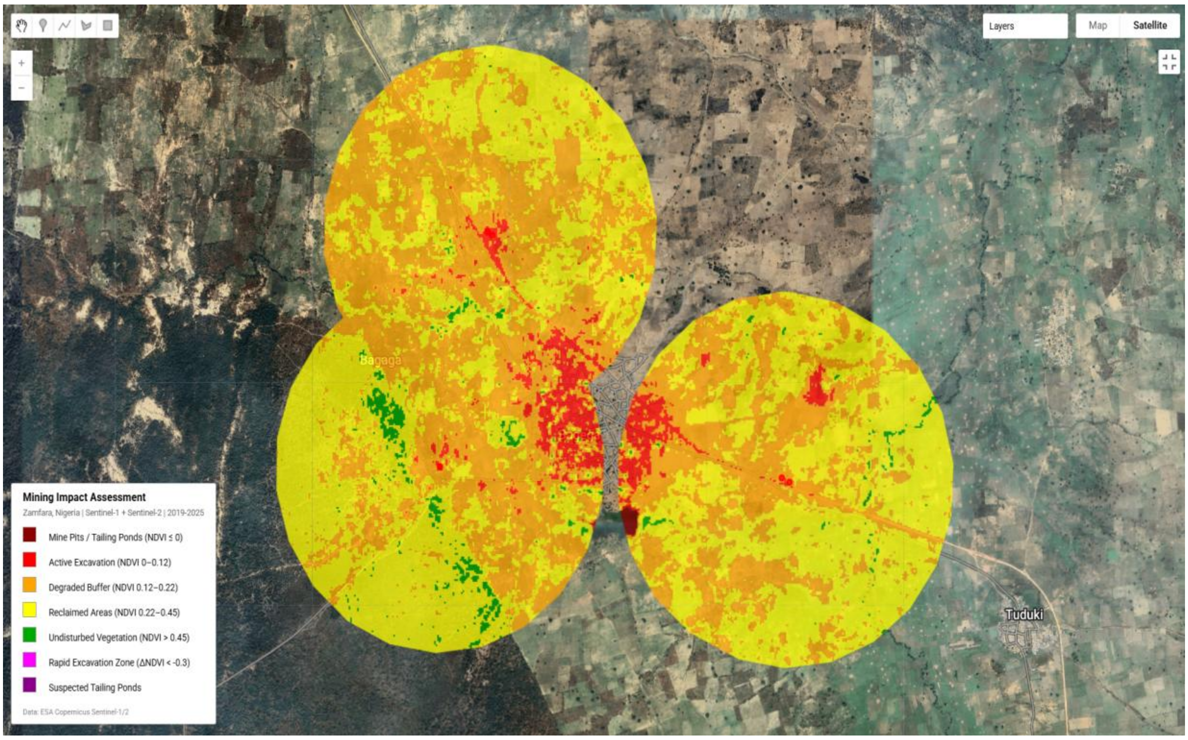

Figure 6c. NDVI visualization for the year 2025

Radar Vegetation Index (RVI) time series from Sentinel-1 independently characterise vegetation structure across zones. Zone 1 RVI rose from 0.499 in 2019 to 0.554 in 2025 (+0.055), with Zone 2 increasing from 0.474 to 0.541 (+0.067) and Zone 3 from 0.480 to 0.549 (+0.069) (Table 4 and Figure 7).

Table 4. Annual Mean RVI

		RVI Time Series		
S/N	**Zone 1 (Direct)**	**Zone 2 (Near)**	**Zone 3 (Far)**	**Year**
1	0.499409268	0.474074035	0.4802273	2019
2	0.517412725	0.496512147	0.508165842	2020
3	0.518385741	0.492997756	0.505721	2021
4	0.497244747	0.477235344	0.486311859	2022
5	0.535231931	0.517582371	0.529748421	2023
6	0.50512797	0.478318467	0.488883933	2024
7	0.554342518	0.5409888	0.54890498	2025

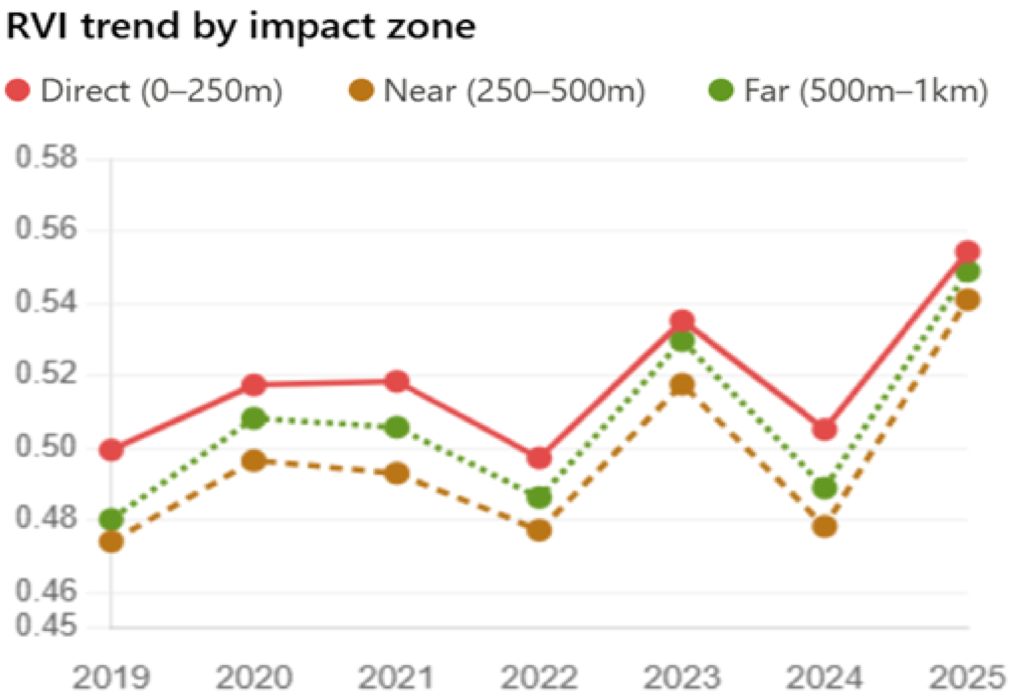

Figure 7. Annual Mean RVI per Buffer Zone, 2019 - 2025

The directional agreement with NDVI, both indices recording net gains over the study period, provides cross-sensor validation of the vegetation trajectory finding and confirms it is not an artefact of harmattan dust suppression of optical reflectance. RVI class mapping reinforces this: bare and mine-pit pixels (RVI < 0.1) declined from 67.46 ha in 2019 to 23.47 ha in 2025 (-65.2%), while healthy vegetation area (RVI > 0.5) increased from 3,051.62 ha to 3,954.53 ha (+29.6%), with a notable peak of 3,703.66 ha in 2023. A notable exception is 2024, when bare pixel area rose to 51.27ha the highest value across the study period except for 2019, and both NDVI and RVI dipped relative to 2023, suggesting a year of renewed disturbance intensity before partial recovery in 2025 (Table 5 and Figure 8).

Table 5. RVI class area statistics by year (2019 - 2025)

RVI Class Area Time Series (ha)					
S/N	**Bare Mine_Ha**	**Degraded**	**Healthy**	**Moderate**	**Year**
1	67.45896978	1439.79275	3051.61905	2702.38982	2019
2	35.52627372	938.6570656	3363.327212	2923.75003	2020
3	20.58482134	847.5933797	3330.537315	3062.54507	2021
4	28.06391224	1004.738656	3008.950375	3219.50764	2022
5	11.05246446	643.7030686	3703.66457	2902.84048	2023
6	51.26769326	1354.166709	3106.915543	2748.91064	2024
7	23.46721198	833.9976347	3954.528265	2449.26747	2025

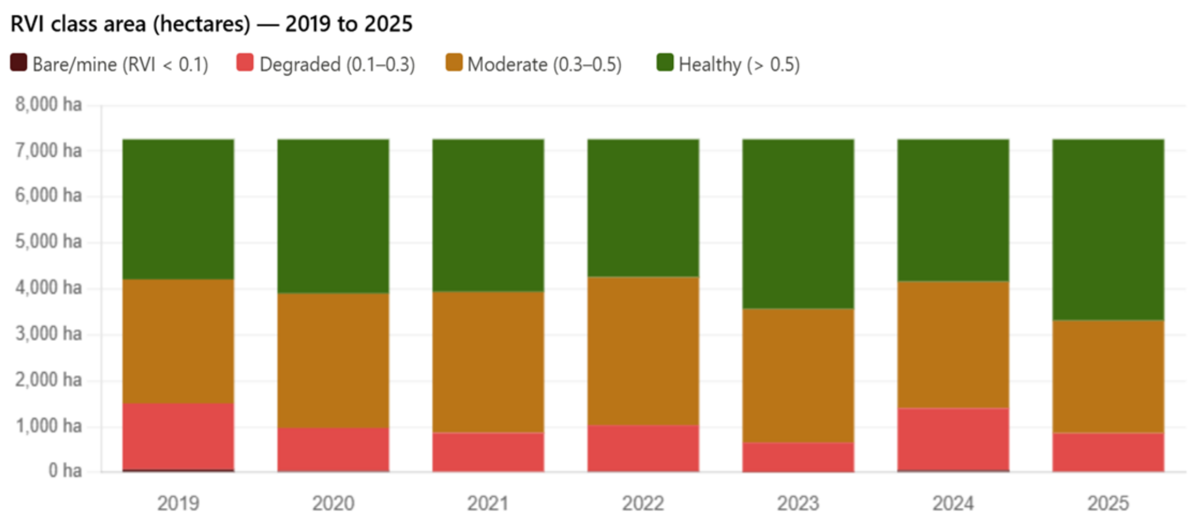

Figure 8. RVI class area statistics (ha) by year (2019–2025)

4.2 Soil Degradation (Bare Soil Index (BSI))

Bare Soil Index (BSI) patterns across the study period reflect the episodic nature of artisanal mining expansion rather than a steady linear degradation trend. Zone 1 mean BSI was relatively stable from 2019 (0.2179) through 2023 (0.2042), fluctuating within a narrow band of approximately ±0.01, before rising sharply to a peak of 0.2532 in 2024, the highest value recorded for any zone in any year, before partially recovering to 0.2211 in 2025. Zone 2 and Zone 3 followed the same pattern: moderate and stable values through 2023, a sharp 2024 peak (0.2614 and 0.2653, respectively), and partial retreat in 2025. The net change from 2019 to 2025 is modest: Zone 1 increased by +0.003, Zone 2 by +0.011, and Zone 3 by +0.012 (Table 6 and Figure 9).

The 2024 BSI peak is the most diagnostically significant feature in the soil degradation record. Its simultaneous appearance across all three buffer zones with the sharpest absolute elevation in Zone 1 points to a landscape-scale disturbance event rather than a localised anomaly. The year 2024 also coincides with the highest RVI bare-pixel area (51.27 ha) and the lowest MNDWI values across the entire time series, suggesting a period of intensified excavation and surface exposure that affected soil moisture, surface water, and vegetation structure in a coordinated way.

Table 6. Annual mean BSI

		BSI Time Series		
S/N	**Zone 1 (Direct)**	**Zone 2 (Near)**	**Zone 3 (Far)**	**Year**
1	0.217881163	0.220261166	0.220290202	2019
2	0.211960878	0.214584023	0.214197856	2020
3	0.207686008	0.211410363	0.211620255	2021
4	0.217852084	0.223269047	0.224771465	2022
5	0.204206061	0.209244859	0.209554874	2023
6	0.253156676	0.261414767	0.265258668	2024
7	0.221146524	0.231031427	0.232087468	2025

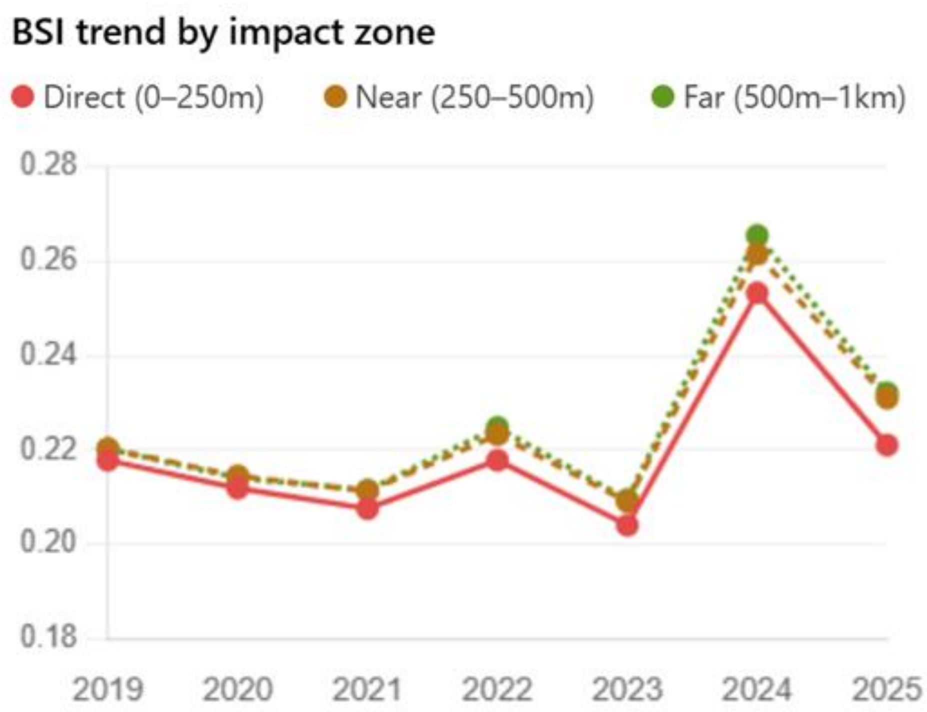

Figure 9: Annual mean BSI per buffer zone, 2019 - 2025

That BSI in Zone 2 and Zone 3 exceeded Zone 1 values in both 2024 and 2025 is counterintuitive if proximity-driven degradation were the sole mechanism; it likely reflects the expansion of mining activity into previously undisturbed areas at greater distances from the original 50 validated sites, consistent with the rotational and outward-spreading character of artisanal pit proliferation in gold-bearing geological belts (Dao *et al*., 2024). The convergence of elevated ΔVV backscatter with BSI peaks in the same years strengthens the attribution of bare soil expansion to active mining disturbance rather than to seasonal soil moisture variability or background dryland desiccation.

4.3 Surface Water Change (Modified Normalised Difference Water Index (MNDWI))

Modified Normalised Difference Water Index (MNDWI) values were consistently negative throughout the study period and across all zones, reflecting the semi-arid character of the landscape and the absence of large permanent water bodies within the buffer extents. Nonetheless, the temporal pattern is diagnostic. Zone 1 MNDWI remained stable from 2019 (-0.453) through 2023 (-0.454) before declining sharply to -0.507 in 2024, a drop of -0.054 in a single year, with partial recovery to -0.492 in 2025. Zone 2 and Zone 3 exhibited parallel declines of -0.069 and -0.081, respectively, between 2023 and 2024, with Zone 3 recording the lowest overall value of -0.550 in 2024. The net change from 2019 to 2025 is -0.039 in Zone 1, -0.057 in Zone 2, and -0.064 in Zone 3 (Table 7 and Figure 10). The counterintuitive pattern of greater MNDWI decline in more distal zones likely reflects the sensitivity of far-buffer water bodies to catchment-level hydrological disruption, including sedimentation of seasonal river channels and diversion of dry-season water flows, rather than direct proximity effects at mine sites.

Table 7: Annual mean MNDWI by zone (2019–2025)

MNDWI Time Series				
S/N	**Zone 1 (Direct)**	**Zone 2 (Near)**	**Zone 3 (Far)**	**Year**
1	-0.452870639	-0.466646952	-0.469536562	2019
2	-0.446373379	-0.460285928	-0.463633345	2020
3	-0.456543223	-0.473591545	-0.477085971	2021
4	-0.457855709	-0.475525632	-0.480605122	2022

MNDWI Time Series				
5	-0.454278982	-0.471542746	-0.475552784	2023
6	-0.506757663	-0.535524054	-0.550420549	2024
7	-0.492148415	-0.523362071	-0.53324287	2025

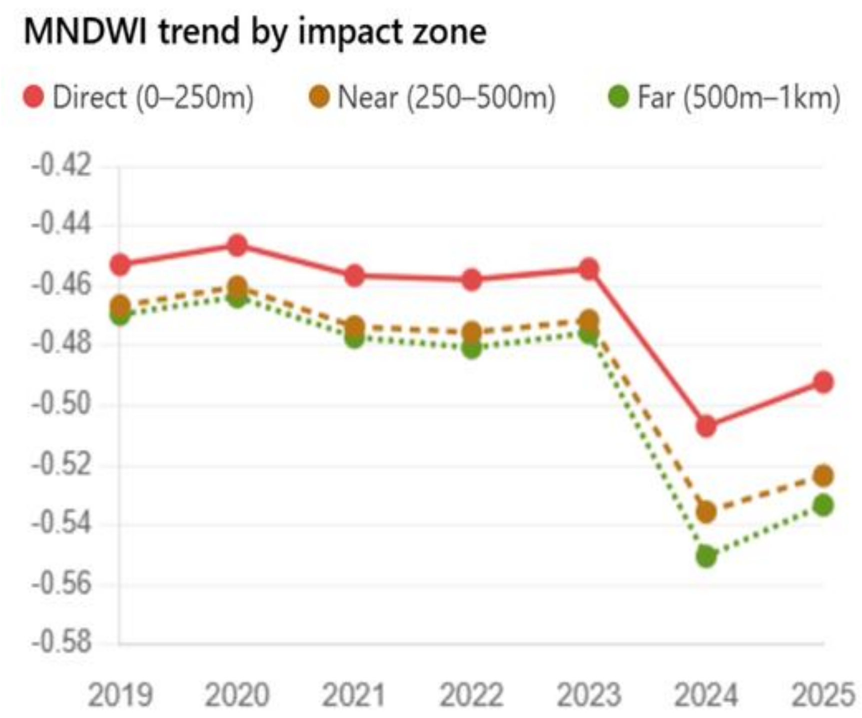

Figure 10. Annual mean MNDWI by zone (2019–2025)

The sharpness of the 2024 decline, synchronous with BSI peaks and the RVI bare-pixel maximum, reinforces the interpretation of 2024 as a year of intensified mining activity with a multi-index environmental signature. The mechanisms most consistent with the observed MNDWI pattern are: turbid tailings sediment altering the spectral signature of residual water bodies, reducing apparent MNDWI values even where water is present; progressive diversion and depletion of ephemeral pools used for artisanal gold processing; and sediment loading of seasonal channels draining mined catchments, which reduces the effective reflectance contrast between water and adjacent soil. Remote sensing of turbid water bodies in mining landscapes has been shown to generate systematically suppressed MNDWI values relative to clear-water benchmarks, making the magnitude of observed decline a likely underestimate of actual surface water deterioration (Ruppen *et al.*, 2023; Zhong *et al.*, 2025). Field water-quality sampling targeting the 2024 and 2025 composite periods is needed to characterise contamination at the specific locations indicated by the tailings pond spectral flag.

4.4 Settlement Expansion (Normalised Difference Built-up Index (NDBI))

Normalised Difference Built-up Index (NDBI) values across all three zones do not show a sustained upward trend consistent with progressive built-up expansion over the study period. Zone 1 values fluctuated between 0.138 (2025) and 0.163 (2019), with a net decline of -0.025. Zone 2 ranged from 0.143 (2025) to 0.173 (2024), also recording a net decline of -0.022 from 2019 to 2025. Zone 3 exhibited a net decline of -0.022. The common pattern across all zones is a relatively low value in 2021 and 2023, a peak in 2024, and the lowest values of the entire series in 2025 (Table 8). The net 2019 – 2025 change is negative in all zones, which does not support a straightforward interpretation of progressive built-up expansion.

Table 8: Annual mean MNDWI by zone (2019 - 2025)

NDBI Time Series				
S/N	**Zone 1 (Direct)**	**Zone 2 (Near)**	**Zone 3 (Far)**	**Year**
1	0.16296378	0.16537417	0.167465235	2019
2	0.160993851	0.164342249	0.166134389	2020
3	0.146077325	0.151378896	0.154862439	2021
4	0.158700414	0.166119926	0.17118963	2022
5	0.14435789	0.149575252	0.152665285	2023
6	0.166792892	0.172862043	0.179443805	2024
7	0.137589398	0.143363177	0.145297519	2025

Several factors may account for this pattern. First, artisanal mining settlements in this region are predominantly composed of impermanent structures, tarpaulins, light metal sheeting, and mud brick whose spectral signatures partially overlap with natural dryland soil and rocky outcrops in Sentinel-2 SWIR and NIR bands, attenuating the NDBI signal relative to conventional built-up environments (Zha *et al*., 2003). Second, the post-2021 recovery in NDVI and RVI across all zones would simultaneously suppress NDBI through increased NIR reflectance, partly masking any real increase in built-up area. Third, the 2024 peak coincides with the BSI peak and MNDWI minimum, suggesting that year reflects broader surface exposure rather than built-up expansion specifically. These interpretive complexities reinforce the need for high-resolution validation data such as aerial or drone imagery to independently assess settlement change around the validated mine sites. The NDBI results should therefore be treated as inconclusive with respect to settlement expansion in this context, and the settlement hypothesis should be evaluated in future work using finer-resolution datasets (Hilson, 2002; Mimba *et al*., 2026).

4.5 Mining Intensity and Environmental Correlation

Pearson correlation analysis was used to examine the relationships between environmental indices and two independent predictors: year, representing cumulative mining expansion, and the Bare Soil Index (BSI), representing the extent of surface exposure. The analysis was conducted for the three buffer zones over the 2019–2025 period. Using both temporal and cross-index approaches enabled the assessment of mining-related environmental change while avoiding circular interpretation.

Temporal Trend Analysis

Temporal correlations revealed clear relationships between mining expansion and environmental conditions across all buffer zones (Table 9A). NDVI exhibited the strongest positive correlations with time $(r = 0.851, 0.835, and\ 0.839\ for\ Zones\ 1-3)$, while MNDWI showed similarly strong negative correlations $(r = -0.839, -0.824, and\ -0.814)$. These results indicate persistent vegetation decline and reductions in surface water throughout the study period. Correlation strengths remained broadly similar across zones, suggesting that environmental change was not restricted to active mining locations but extended across the wider landscape.

BSI recorded moderate positive correlations with time $(r = 0.539 - 0.556)$, reflecting progressive expansion of exposed surfaces. RVI also showed moderate positive correlations $(r = 0.454 - 0.524)$, although the relationship was weaker than that observed for the optical indices. In contrast, NDBI exhibited negligible correlations with time $(r = -0.158\ to\ -0.068)$, indicating limited evidence of systematic built-up expansion within the study buffers during the observation period.

Table 9A. Temporal correlations between year and environmental indices across the three impact zones (2019–2025)

Index	Zone 1 *r*	Zone 1 R^2	Zone 2 *r*	Zone 2 R^2	Zone 3 *r*	Zone 3 R^2
NDVI	+0.851	0.723	+0.835	0.697	+0.839	0.704
MNDWI	−0.839	0.704	−0.824	0.679	−0.814	0.663
BSI	+0.539	0.291	+0.556	0.309	+0.547	0.299
RVI	+0.512	0.262	+0.454	0.206	+0.524	0.274
NDBI	−0.158	0.025	−0.068	0.005	−0.097	0.009

Proxy variable: year index (1 = 2019, 7 = 2025), representing cumulative mining expansion. Zone 1 = 0 – 250 m (direct impact); Zone 2 = 250 – 500 m (near impact); Zone 3 = 500 m–1 km (far impact). Strength thresholds: strong |r| ≥ 0.70; moderate 0.40 ≤ |r| < 0.70; weak |r| < 0.40.

Cross-Index Analysis

Cross-index analysis identified strong relationships between BSI and several environmental indicators (Table 9B). The strongest association occurred between BSI and MNDWI, with correlation coefficients ranging from -0.857 to -0.870 across the three zones. Corresponding R^2 values (0.734 – 0.757) indicate a close relationship between increasing bare soil exposure and declining surface water conditions. The relationship strengthened slightly with distance from mining sites, suggesting that hydrological responses extend beyond areas of direct excavation.

Moderate positive correlations were observed between BSI and NDBI ($r = 0.603 - 0.650$). The highest value occurred in Zone 2 (R^2 = 0.423), indicating a closer association between exposed surfaces and built-up features within the near-impact zone. This pattern aligns with field observations showing that mining-support infrastructure is often concentrated outside active excavation areas.

The relationship between BSI and NDVI increased progressively from Zone 1 (R^2 = 0.167) to Zone 3 (R^2 = 0.287). The weaker association in the direct impact zone likely reflects greater spatial heterogeneity arising from excavation pits, spoil deposits, and processing areas. In the outer buffer, vegetation response appeared more spatially uniform, resulting in a stronger statistical relationship.

BSI and RVI showed weak correlations across all zones ($r = -0.190\ to\ -0.210$).This outcome reflects differences in the physical properties measured by each index. Whereas BSI responds primarily to soil exposure and surface reflectance characteristics, RVI is influenced by vegetation structure and moisture-related scattering effects. The weak association therefore indicates that the two indices capture different dimensions of environmental change rather than providing redundant information.

Table 9B: Cross-index correlations between BSI and environmental indices across the three impact zones.

Index pair	Zone 1 *r*	Zone 1 R^2	Zone 2 *r*	Zone 2 R^2	Zone 3 *r*	Zone 3 R^2
BSI → MNDWI	−0.857	0.734	−0.865	0.749	−0.870	0.757
BSI → NDBI	+0.603	0.364	+0.650	0.423	+0.641	0.411
BSI → NDVI	+0.409	0.167	+0.484	0.234	+0.535	0.287
BSI → RVI	−0.207	0.043	−0.210	0.044	−0.190	0.036

Predictor: BSI (Sentinel-2 bare soil index, annual zone means). Self-correlation (BSI → BSI) excluded. Zone definitions as in Table 9A.

Optical and SAR Responses to Mining Activity

The results reveal stronger temporal correlations for the optical indices than for the SAR-derived RVI. NDVI $(r = 0.835 - 0.851)$ and MNDWI $(r = -0.814\ to\ -0.839)$ consistently exceeded the correlations observed for RVI $(r = 0.454 - 0.524)$. Under the dry-season compositing strategy adopted in this study, optical imagery provided a clearer representation of vegetation and surface water dynamics. SAR data remain valuable because they are less affected by atmospheric conditions and can provide observations during periods when optical imagery is unavailable. The findings therefore support the complementary use of optical and SAR datasets rather than the superiority of one sensor type over the other.

Spatial Pattern of Environmental Change

Comparison of the three buffer zones indicates that mining-related environmental impacts operate at multiple spatial scales. Strong temporal relationships between year and both NDVI and MNDWI were observed throughout the study area, demonstrating a consistent trajectory of environmental degradation. At the same time, several cross-index relationships, particularly BSI – MNDWI and BSI – NDVI, became stronger with distance from mining locations. This pattern suggests that while direct physical disturbance is concentrated around excavation sites, its ecological and hydrological effects extend across the broader landscape.

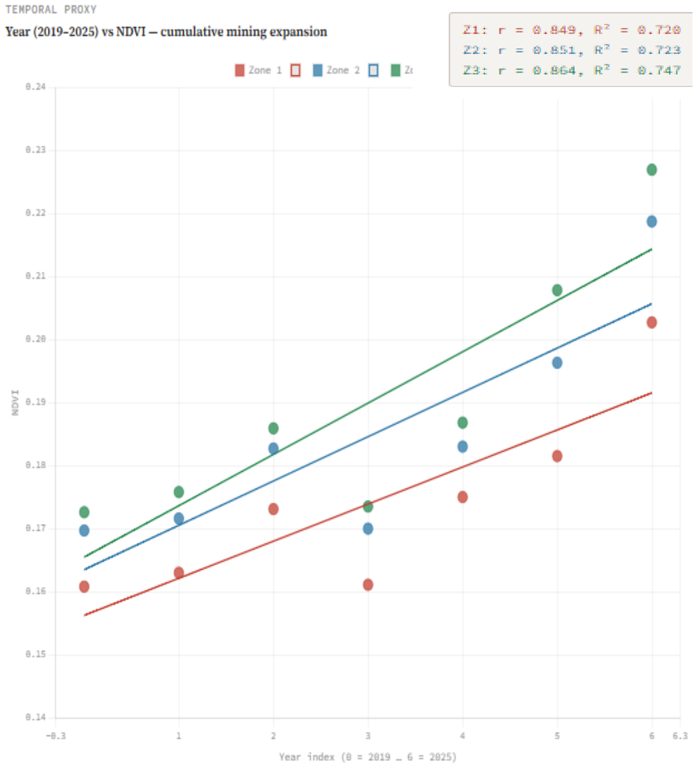

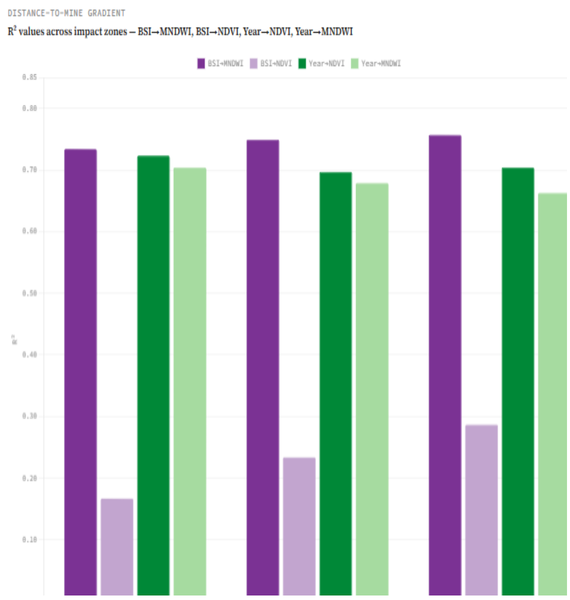

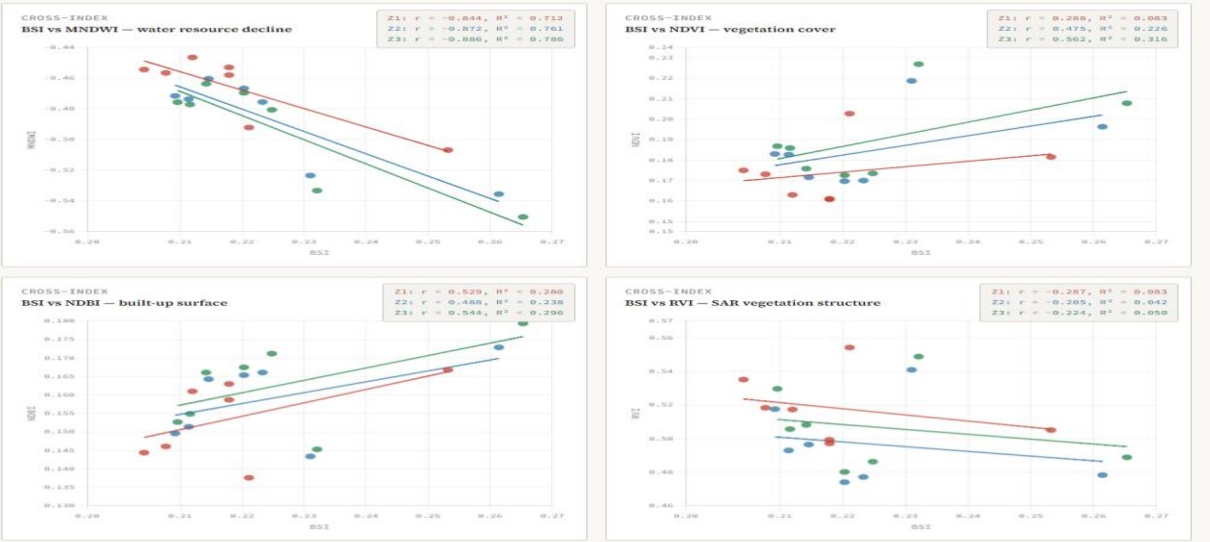

Figure 11: Scatter plots showing temporal and cross-index relationships between mining intensity indicators and environmental indices across the three impact zones.

5.0 CONCLUSION

This study provides the first systematic multi-temporal assessment of environmental change across the artisanal and small-scale gold mining (ASGM) corridor of Anka, Bukkuyum, Maru, and Talata Mafara Local Government Areas in Zamfara State, Nigeria. Using a SAR–optical data fusion framework implemented in Google Earth Engine (GEE), annual environmental conditions were evaluated between 2019 and 2025 at 10 m spatial resolution.

Findings indicate that the mining landscape is characterised by concurrent disturbance and recovery rather than a unidirectional pattern of degradation. Mine-pit extent increased by 260%, from 2.54 ha to 9.16 ha, while reclaimed and naturally revegetating areas expanded by 227%, from 945.89 ha to 3,096.15 ha. Increasing NDVI and RVI values across all buffer zones suggest that vegetation recovery, influenced largely by interannual rainfall variability, occurs alongside continued mining expansion. This highlights the limitations of single-date vegetation assessments, which may fail to distinguish mining impacts from broader climatic influences.

Temporal trend analysis revealed persistent environmental change throughout the study period. NDVI exhibited the strongest positive temporal relationships $(r = 0.835 - 0.851;\ R^2 = 0.697 - 0.723)$, while MNDWI recorded the strongest negative trends $(r = -0.814\ to\ -0.839;\ R^2 = 0.663 - 0.704)$, indicating sustained vegetation transformation and declining surface-water conditions. The consistency of these relationships across the 250 m, 500 m, and 1 km buffer zones demonstrates that mining impacts extend beyond active excavation sites and operate at a broader landscape scale. BSI showed moderate positive trends associated with episodic surface exposure, whereas NDBI displayed weak and inconsistent relationships, suggesting limited suitability for monitoring temporary mining settlements in this environment.

The 2024 dry season emerged as the most significant disturbance period within the time series. Peak BSI values, minimum MNDWI values, and the largest RVI-derived bare-surface extent occurred simultaneously across all buffer zones, providing strong evidence of intensified environmental stress. The convergence of optical and SAR indicators during this period underscores the value of a multi-index approach for identifying disturbance events that may not be apparent from a single dataset.

Cross-index analysis further revealed strong inverse relationships between BSI and MNDWI ($R^2 = 0.734 - 0.757$), indicating that increasing soil exposure is closely associated with declining surface-water conditions. The strengthening of this relationship with distance from mine sites suggests that hydrological impacts propagate beyond areas of direct excavation through sediment transport and catchment-scale runoff processes. These findings identify surface-water systems as among the most vulnerable environmental components affected by ASGM activities in the Zamfara mining corridor.

The study also demonstrates the complementary roles of optical and SAR observations. Sentinel-2-derived indices were more sensitive to long-term vegetation and water dynamics under the dry-season compositing strategy, while the Radar Vegetation Index (RVI) provided cloud-independent information on structural vegetation change and land-surface disturbance. Rather than serving as alternatives, the two sensor systems provide complementary evidence for environmental monitoring in dryland regions.

Methodologically, three contributions emerge. First, the four-stage mine-site validation framework combining NGSA mineral resource mapping, NMCO permit records, documentary evidence, and Google Earth Pro interpretation offers a practical approach for identifying and validating ASGM locations. Second, the GEE-based workflow demonstrates the feasibility of long-term, multi-sensor environmental monitoring using freely available datasets and reproducible analytical procedures. Third, the integration of multiple indices over seven years reveals environmental trajectories that would not be captured through single-index or endpoint analyses.

Future work should focus on field-based validation of remotely sensed observations, targeted water-quality and heavy-metal assessments around identified disturbance hotspots, higher-resolution mapping of mining settlements, and the integration of socioeconomic indicators to better understand human vulnerability within ASGM-affected communities. Continued monitoring beyond 2025 is necessary to document post-disturbance recovery, assess the cumulative effects of ASGM activities, and strengthen the evidence base for environmental management in mining-affected landscapes of northwestern Nigeria and the broader Nigerian mining sector.

ACKNOWLEDGEMENTS

The authors gratefully acknowledge the European Space Agency for providing open access to Sentinel-1 and Sentinel-2 imagery through the Copernicus Open Access Hub, and Google LLC for the Earth Engine cloud computing platform. The authors further acknowledge the Nigerian Geological Survey Agency (NGSA) for supplying the Mineral Resources Map of Nigeria that supported this research. The authors also appreciate the contribution of Dr. Mohammed Idrees for guidance and improvement of the research, and all individuals and institutions that supported this research.

REFERENCES

Ado, S. J., Ejidike, B. N., Adetola, B., & Olaniyi, O. E. (2022). Evaluation of Land Use and Land Cover Changes in the Gold Mining Enclaves of Zamfara Sahel, Nigeria. *Journal of Applied Sciences and Environmental Management*, *26*(2). https://doi.org/10.4314/jasem.v26i2.22

Aryee, B. N. A., Ntibery, B. K., & Atorkui, E. (2003). Trends in the Small-Scale Mining of Precious Minerals in Ghana: A Perspective on Its Environmental Impact. *Journal of Cleaner Production*, *11*(2), 131–140. https://doi.org/10.1016/S0959-6526(02)00043-4

Balogun, B. O., Ojo, A. G., Aluko, O. E., & Alage, L. I. (2024). Assessment of Mining-Induced Land Degradation in Ile-Ife, Osun State, Nigeria. *Osun Geographical Review*, *6*(1). https://journals.uniosun.edu.ng/ogr/article/view/159

Bansah, K. J., Yalley, A. B., & Dumakor-Dupey, N. (2018). The Hazardous Nature of Small-Scale Underground Mining in Ghana. *Journal of Sustainable Mining*, *17*(1), 1–10. https://doi.org/10.1016/j.jsm.2017.12.003

Barde, B. G., Adeleye, A. O., Oladeji, A. A., & Duhu, Y. B. (2024). Heavy Metals Pollution and Ecological Risk Assessment Around Artisanal Gold Mines in Zamfara, Nigeria. *Environmental Analysis, Health and Toxicology*, *39*(2), e2024016. https://doi.org/10.5620/eaht.2024016

Bartrem, C., von Lindern, I., von Braun, M., & Tirima, S. (2022). Climate Change, Conflict, and Resource Extraction: Analyses of Nigerian Artisanal Mining Communities and Ominous Global Trends. *Annals of Global Health*, *88*(1). https://doi.org/10.5334/aogh.3547

Blanche, M. F., Dairou, A. A., Juscar, N., Romarice, O. M. F., Arsene, M., Bernard, T. L., & Leroy, M. N. L. (2024). Assessment of Land Cover Degradation Due to Mining Activities Using Remote Sensing and Digital Photogrammetry. *Environmental Systems Research*, *13*(1), 41. https://doi.org/10.1186/s40068-024-00372-5

Castaldi, F., Halil Koparan, M., Wetterlind, J., Žydelis, R., Vinci, I., Özge Savaş, A., Kıvrak, C., Tunçay, T., Volungevičius, J., Obber, S., Ragazzi, F., Malo, D., & Vaudour, E. (2023). Assessing the Capability of Sentinel-2 Time-Series to Estimate Soil Organic Carbon and Clay Content at Local Scale in Croplands. *ISPRS Journal of Photogrammetry and Remote Sensing*, *199*, 40–60. https://doi.org/10.1016/j.isprsjprs.2023.03.016

Couttenier, M., Di Rollo, S., Inguere, L., Mohand, M., & Schmidt, L. (2022). Mapping Artisanal and Small-Scale Mines at Large Scale from Space with Deep Learning. *PLOS ONE*, *17*(9), e0267963. https://doi.org/10.1371/journal.pone.0267963

Dao, R. A. I., Ilboudo, H., & Baratoux, D. (2024). Structural Controls of the Expansion of Small-Scale Artisanal Gold of Bouda Area (Kaya-Goren Green Belt, Burkina Faso) From Remote Sensing. *Earth and Space Science*, *11*(3), e2023EA003217. https://doi.org/10.1029/2023EA003217

Gao, Q., Zribi, M., Escorihuela, M. J., Baghdadi, N., & Segui, P. Q. (2018). Irrigation Mapping Using Sentinel-1 Time Series at Field Scale. *Remote Sensing*, *10*(9), 1495. https://doi.org/10.3390/rs10091495

Gorelick, N., Hancher, M., Dixon, M., Ilyushchenko, S., Thau, D., & Moore, R. (2017). Google Earth Engine: Planetary-Scale Geospatial Analysis for Everyone. *Remote Sensing of Environment*, *202*, 18–27. https://doi.org/10.1016/j.rse.2017.06.031

Hilson, G. (2002). Small-Scale Mining and Its Socio-Economic Impact in Developing Countries. *Natural Resources Forum*, *26*(1), 3–13. https://doi.org/10.1111/1477-8947.00002

Hu, X., Li, L., Huang, J., Zeng, Y., Zhang, S., Su, Y., Hong, Y., & Hong, Z. (2024). Radar Vegetation Indices for Monitoring Surface Vegetation: Developments, Challenges, and Trends. *Science of The Total Environment*, *945*, 173974. https://doi.org/10.1016/j.scitotenv.2024.173974

Ibukun, J. A., Olubaju, A. E., Thomas, S. F., Sodipo, E. O., Akinbiola, S. A., Rebouh, N. Y., Said, Y., & Tariq, A. (2025). Assessing Vegetation Degradation and Thermal Effects of Artisanal Small-Scale Mining Using Remote Sensing Time Series Data. *Land Degradation & Development*, *37*(6), 2267–2289. https://doi.org/10.1002/ldr.70244

Isah, A., Akinbiyi, O. A., Hansen-Ayoola, A., Ayajuru, N. C., Muraina, T. A., & Rafiu, F. O. (2025). Heavy Metal Contamination Driven by Artisanal Gold Mining in the Ile-Ife–Ilesha Schist Belt, Nigeria: Geospatial Assessment of Pollution Sources and Hotspots. *Environmental Monitoring and Assessment*, *197*(10), 1081. https://doi.org/10.1007/s10661-025-14561-x

Lambin, E. F., & Strahler, A. H. (1994). Change-Vector Analysis in Multitemporal Space: A Tool to Detect and Categorize Land-Cover Change Processes Using High Temporal-Resolution Satellite Data. *Remote Sensing of Environment*, *48*(2), 231–244. https://doi.org/10.1016/0034-4257(94)90144-9

Mandal, D., Kumar, V., Ratha, D., Dey, S., Bhattacharya, A., Lopez-Sanchez, J. M., McNairn, H., & Rao, Y. S. (2020). Dual Polarimetric Radar Vegetation Index for Crop Growth Monitoring Using Sentinel-1 SAR Data. *Remote Sensing of Environment*, *247*, 111954. https://doi.org/10.1016/j.rse.2020.111954

Mimba, M. E., Fils, S. C. N., Tibang, E. E. B., Ondoa, G. E. M., Bachirou, D., & Ateh, K. I. (2026). Artisanal and Small-Scale Gold Mining–Driven Settlement Expansion and Socio-Environmental Pressures in East Cameroon, Sub-Saharan Africa. *Discover Geoscience*, *4*(1), 98. https://doi.org/10.1007/s44288-026-00468-8

Ngom, N. M., Baratoux, D., Bolay, M., Dessertine, A., Abass Saley, A., Baratoux, L., Mbaye, M., Faye, G., Yao, A. K., & Kouamé, K. J. (2022). Artisanal Exploitation of Mineral Resources: Remote Sensing Observations of Environmental Consequences, Social and Ethical Aspects. *Surveys in Geophysics*, *44*(1), 225–247. https://doi.org/10.1007/s10712-022-09740-1

Ngom, N. M., Mbaye, M., Baratoux, D., Baratoux, L., Catry, T., Dessay, N., Faye, G., Sow, E. H., & Delaitre, E. (2020). Mapping Artisanal and Small-Scale Gold Mining in Senegal Using Sentinel 2 Data. *GeoHealth*, *4*(12), e2020GH000310. https://doi.org/10.1029/2020GH000310

Oseikhuemen, B. V., Christopher Simon Dalom, & Esharive Ogaga. (2025). Environmental Impact of Artisanal Gold Mining in Nigeria: A Review. *Dutse Journal of Pure and Applied Sciences*, *11*(3a), 373–383. https://doi.org/10.4314/dujopas.v11i3a.33

Phiri, D., Simwanda, M., Salekin, S., Nyirenda, V. R., Murayama, Y., & Ranagalage, M. (2021). Sentinel-2 Data for Land Use and Land Cover Mapping: A Review. *Remote Sensing*, *13*(3), 516. https://doi.org/10.3390/rs13030516

Ruppen, D., Runnalls, J., Tshimanga, R. M., Wehrli, B., & Odermatt, D. (2023). Optical Remote Sensing of Large-Scale Water Pollution in Angola and DR Congo Caused by the Catoca Mine Tailings Spill. *International Journal of Applied Earth Observation and Geoinformation*, *118*, 103237. https://doi.org/10.1016/j.jag.2023.103237

Salih, A. A. M., Ganawa, E. T., & Elmahl, A. A. (2017). Spectral Mixture Analysis and Change Vector Analysis Methods for Monitoring and Mapping Land Degradation/Desertification in Arid and Semiarid Areas (Sudan), Using Landsat Imagery. *Egyptian Journal of Remote Sensing and Space Sciences*, *20*(S1), S21–S29. https://doi.org/10.1016/j.ejrs.2016.12.008

Sambe, L. N., Adeofun, C. O., Oyedepo, J. A., Osunmadewa, B. A., & Soaga, J. A. (2026). Evaluation of Desertification Dynamics in the Frontline States of Northern Nigeria: Environmental and

Socioeconomic Impacts. *Environmental Research Communications*, *8*(2), 025002. https://doi.org/10.1088/2515-7620/ae322b

Sengani, D., Ramoelo, A., & Archer, E. (2023). A Review of Fusion Framework Using Optical Sensors and SAR Imagery to Detect and Map Land Degradation and Sustainable Land Management in the Semi-Arid Regions. *Geocarto International*, *38*(1), 2278325. https://doi.org/10.1080/10106049.2023.2278325

Torres, R., Snoeij, P., Geudtner, D., Bibby, D., Davidson, M., Attema, E., Potin, P., Rommen, B., Floury, N., Brown, M., Traver, I. N., Deghaye, P., Duesmann, B., Rosich, B., Miranda, N., Bruno, C., L'Abbate, M., Croci, R., Pietropaolo, A., & Rostan, F. (2012). GMES Sentinel-1 Mission. *Remote Sensing of Environment*, *120*, 9–24. https://doi.org/10.1016/j.rse.2011.05.028

Tucker, C. J. (1979). Red and Photographic Infrared Linear Combinations for Monitoring Vegetation. *Remote Sensing of Environment*, *8*(2), 127–150. https://doi.org/10.1016/0034-4257(79)90013-0

Xu, H. (2006). Modification of Normalised Difference Water Index (NDWI) to Enhance Open Water Features in Remotely Sensed Imagery. *International Journal of Remote Sensing*, *27*(14), 3025–3033. https://doi.org/10.1080/01431160600589179

Zha, Y., Gao, J., & Ni, S. (2003). Use of Normalized Difference Built-up Index in Automatically Mapping Urban Areas from TM Imagery. *International Journal of Remote Sensing*, *24*(3), 583–594.

Zhong, A., Wang, Z., & Gen, Y. (2025). Research on water body information extraction and monitoring in high water table mining areas based on Google Earth Engine. *Scientific Reports*, *15*(1), 12133. https://doi.org/10.1038/s41598-025-97018-y